

Limits to Extracting Neutron-Star Physics Constraints from *NICER* Pulse Profiles

TOLGA GÜVER,^{1,2,3} DIMITRIOS PSALTIS,³ FERYAL ÖZEL,³ AND TONG ZHAO³

¹*Istanbul University, Science Faculty, Department of Astronomy and Space Sciences, Beyazıt, 34119, İstanbul, Türkiye*

²*Istanbul University Observatory Research and Application Center, Istanbul University 34119, İstanbul, Türkiye*

³*School of Physics, Georgia Institute of Technology, 837 State Street NW, Atlanta, GA 30332, USA*

ABSTRACT

Modeling energy-dependent X-ray pulse profiles from rotation-powered millisecond pulsars observed with *NICER* has emerged as a promising avenue for measuring neutron star radii and probing the equation of state of cold, ultra-dense matter. However, pulse profile models have often required an unwieldy number of parameters to account for complex surface emission geometries, introducing the risk of overfitting and degeneracies. To explore the number of model parameters that can be inferred uniquely, we perform a quantitative assessment of the information content in X-ray pulse profiles by applying Fourier methods. We determine the number of independent observables that can be reliably extracted from the pulse shapes, as well as from complementary X-ray spectral data obtained with *XMM-Newton*, for key *NICER* targets. Our analysis provides a framework for evaluating the match between model complexity and data constraints. It also demonstrates the importance of incorporating in the model the pulsed components of the magnetospheric non-thermal emission, which often contributes significantly to the observed spectra. Our results highlight limitations in previous inferences of neutron-star radii from *NICER* observations, which have incorporated model complexity not supported by the data.

Keywords: Millisecond pulsars; X-ray astronomy; Neutron stars

1. INTRODUCTION

Neutron stars have been one of the key astrophysical sources for understanding the nature of cold matter at or above nuclear saturation density (see, e.g., [Lattimer & Prakash 2001](#); [Özel & Freire 2016](#)). Because the Tolman-Oppenheimer-Volkoff equations allow us to relate the macroscopic measurables, namely the masses and radii, to the details of the equation of state of matter inside neutron stars ([Tolman 1939](#); [Oppenheimer & Volkoff 1939](#)), astrophysical observations of these objects have played a central role in constraining dense matter physics. Neutron stars have especially been observed in radio, X-rays, and gamma-ray bands. Although the radio and gamma-ray emission of neutron stars generally emanate not from the surface but rather from the magnetosphere, exploiting the general relativistic effects in the timing observations of binary millisecond pulsars has proven to be a fruitful and precise tool for determining the masses of neutron stars in binary systems (see e.g. [Lorimer 2008](#); [Özel & Freire 2016](#)). However, obtaining independent measurements of radii has been significantly more challenging.

One approach has involved X-ray observations of thermonuclear X-ray bursts ([Lewin et al. 1993](#)) that reach the Eddington luminosity. In such cases, the X-ray flux measured at or around the time of the observed contraction of the photosphere is related to the mass and radius of the neutron star ([Paradijs 1978](#); [Paradijs & Lewin 1978](#); [Damen et al. 1990](#); [Paradijs & Lewin 1993](#)). Furthermore, during the cooling tails of these events, there is again a relationship between the apparent emitting area and the mass and the radius of the neutron star ([van Paradijs 1982](#); [Paradijs & Lewin 1993](#)). Observations of bursting neutron stars with the Proportional Counter Array (PCA) onboard the Rossi X-ray Timing Explorer (RXTE) employing this technique resulted in multiple radius measurements in the 10 – 11.5 km range ([Özel et al. 2009](#); [Güver et al. 2010a,b](#); [Özel et al. 2010](#); [Steiner et al. 2010, 2013](#); [Özel et al. 2016](#)).

Another approach has utilized imaging X-ray telescopes with very low backgrounds, which allowed studies of the surface thermal X-ray emission from neutron stars to constrain their masses and radii. Specifically, observations of low mass X-ray binaries in quiescence in globular clusters have yielded correlated constraints

that also favor smaller radii (see, e.g., Heinke et al. 2014; Bogdanov et al. 2016; Shaw et al. 2018; Echiburú et al. 2020).

A third avenue toward constraining neutron star masses and radii is through modeling the energy-dependent X-ray pulse profiles (see, e.g., Pechenick et al. 1983; Weinberg et al. 2001; Psaltis & Özel 2014; Watts et al. 2016). Such measurements require sensitivity to soft X-rays, large effective area, and very high time resolution, all of which are provided by the Neutron Star Interior and Composition Explorer (*NICER*, Gendreau et al. 2012). Long *NICER* observations of PSR J0437–4715, PSR J0030+0451, PSR J1231–1411, PSR J0740+6620 allowed for their X-ray pulse profiles to be measured sensitively. Subsequent studies modeled the shapes, locations, and numbers of hot spots on the surfaces of these pulsars and, based on these models, derived constraints on their masses and radii (Miller et al. 2019; Dittmann et al. 2024; Riley et al. 2019, 2021; Salmi et al. 2024a,b; Choudhury et al. 2024). In the majority of these studies, complex and often unexpected geometries were inferred, leading to a proliferation of model parameters to describe the shapes and locations of multiple hot spots on the stellar surface.

The ability of an observed pulse profile to uniquely constrain the surface emission characteristics and, therefore, the stellar mass and radius relies heavily on the complexity observed in the pulse profile and the mapping of its features to the surface emission. For example, if a pulse profile is well described by a simple sinusoid (within the measurement uncertainties), it provides at most two pieces of information: amplitude and phase. Such limited information may be insufficient to constrain a model with a complex emission structure and will lead to overfitting and degeneracies. This raises a fundamental question: what is the information content of an observed pulse profile, and how does it compare to the number of parameters used to model it?

In this paper, we use Fourier methods to determine the number of model parameters that can be measured from a combination of the pulse profiles observed with *NICER* and the X-ray spectral data observed with *XMM-Newton* for the primary *NICER* targets. In §2 we outline the methodology, in §3-5 we present our analysis of the data, and in §6, we discuss our findings.

2. METHODOLOGY

Pulsed emission from millisecond pulsars in the X-rays is most likely caused by returning magnetospheric relativistic charged particles causing temperature anisotropies on the surface (see e.g., Ruderman & Sutherland 1975; Philippov et al. 2015; Brambilla et al.

2018; Bauböck et al. 2019) as well as non-thermal magnetospheric processes. Although the detailed nature and spin-phase dependence of the non-thermal emission is not clear, the observational properties of the thermal component(s) have been studied extensively (see e.g., Zavlin & Pavlov 2002; Bogdanov et al. 2007, 2008; Bogdanov & Grindlay 2009; Özel 2013; Bogdanov 2013).

Reflecting mainly the magnetic field configuration and the properties of the atmosphere, heating anisotropies caused by return currents can create hot spots with different sizes and temperatures at different locations on the surface, which then form the observed pulsed emission as the neutron star rotates. The shape of the pulse profile depends on the number, size, temperature, and relative orientation of the different hot spots. Each one contributes a distinct component to the X-ray spectrum and introduces a unique set of Fourier modes to the photon flux as a function of spin phase. Furthermore, relativistic effects caused by the strong gravitational field of the neutron star reshape this pulsed emission, resulting in the observed pulse profiles (Pechenick et al. 1983; Poutanen & Beloborodov 2006; Morsink & Leahy 2011; Psaltis & Özel 2014).

We write the contribution of the i -th surface component to the flux at energy E and spin phase ϕ as

$$F_i(E, \phi) = \sum_{n=0}^{\infty} \{A_{in}(E) \cos[n(\phi - \phi_i)] + B_{in}(E) \sin[n(\phi - \phi_i)]\} \quad (1)$$

where A_{in} and B_{in} are the amplitudes of the cosine and sine Fourier modes and ϕ_i is the central azimuth of the hot spot that generates this spectral component with respect to some fiducial value. For slowly spinning neutron stars, the sine terms in this expansion are subdominant (see, e.g., Poutanen & Beloborodov 2006) and, for brevity, we will not carry them hereafter. The total flux from all S surface components is then

$$F(E, \phi) = \sum_{i=1}^S \sum_{n=0}^{\infty} A_{in}(E) \cos[n(\phi - \phi_i)] . \quad (2)$$

Expanding the cosine terms, we can write this as

$$F(E, \phi) = \sum_{n=0}^{\infty} \sum_{i=1}^S [A_{in}(E) \cos(n\phi_i) \cos(n\phi) + A_{in}(E) \sin(n\phi_i) \sin(n\phi)] \quad (3)$$

or equivalently

$$F(E, \phi) = A_0(E) + \sum_{n=1}^{\infty} [A_n(E) \cos(n\phi) + B_n(E) \sin(n\phi)] , \quad (4)$$

where

$$A_0(E) = \sum_{i=1}^S A_{i0}(E) \quad (5)$$

$$A_n(E) = \sum_{i=1}^S A_{in}(E) \cos(n\phi_i) \quad (6)$$

$$B_n(E) = \sum_{i=1}^S A_{in}(E) \sin(n\phi_i) . \quad (7)$$

Equation (4) is a complete expression that can describe any pulse profile of arbitrary complexity. In practice, however, an infinite number of Fourier components are not required to describe or supported by the actual data, both because of the signal-to-noise of the data and of the degree of the intrinsic complexity of the pulse profiles. As a result, the sum of Fourier modes in Eq. (4) terminates at some $N = N_{\max}$. In §3, we use *NICER* data to quantify the number of independent Fourier components that can be measured at different photon energies for the primary targets. In §4, we use *XMM-Newton* data to determine the number S of independent spectral components arising from the stellar surface. We combine the results of these two analyses in §5 to quantify the number of model parameters that can be meaningfully inferred from the current *NICER* data.

We focus our attention to PSR J0437–4715 given the fact that it is the brightest among all the pulsars used for pulse profile modeling (Guillot et al. 2016). In Appendix B, we repeat the same analysis for the remaining sources PSR J0030+0451, PSR J0740+6620, PSR J1231–1411, which have been observed for pulse profile modeling with *NICER*.

PSR J0437–4715 is the closest pulsar with a known distance of 156.96 ± 0.11 pc (Reardon et al. 2024). It was discovered during the Parkes radio pulsar survey (Johnston et al. 1993) and as an X-ray source with ROSAT (Becker & Trümper 1993). Being the closest, brightest millisecond pulsar with a precise mass measurement ($M = 1.418 \pm 0.044 M_{\odot}$, Reardon et al. 2024) made PSR J0437–4715 one of the prime targets for *NICER*.

Its broadband X-ray spectrum has also been studied extensively. Using data from ROSAT, *XMM-Newton*, and *NuSTAR*, Guillot et al. (2016) provided detailed constraints on the number and parameters of the X-ray spectral components. They found that the 0.1–20 keV band data are best described with three thermal components and one power-law component, and determined the amount of absorption by the interstellar medium. Most importantly, thanks to *NuSTAR* observations, they detected pulsed emission from PSR J0437–

4715 with a pulse fraction of $24 \pm 6\%$ in the 2–20 keV band. Guillot et al. (2016) also demonstrated that the contribution from the power-law component produces comparable flux to that of the surface emission at energies above 2 keV.

3. NICER DATA AND PULSE PROFILES

We obtained the *NICER* data extracted by Choudhury et al. (2024) from the Zenodo archive¹. Specifically we use the file, *j0437_3c50_cl_evt_merged_phase.txt*, which contains time of arrivals (ToAs) of each event as well as their PI (energies) and the spin phase values, such that an energy dependent pulse profile can be easily generated for the data obtained with *NICER* from 2017 July 6 to 2021 October 11. For the background, we used the *rj0437_3c50_bg_pha_spec.txt* file. This file contains channels, count rates, and the statistical errors, as calculated by the 3C50 model.

Since the full event file contains the total number of events arriving at the detectors throughout the numerous observations, it is necessary to calculate the total number of background events in each energy range. For that purpose, we used the total exposure time of 1.328 Ms (Choudhury et al. 2024). Within the 0.3–3.0 keV range, the event file has a total of 2,095,698 events. In the same energy range, the 3C50 background model predicts 0.495 counts s^{-1} , which results in a total of 657,677 background events. When calculating the pulse profiles, we divided the 0.3 – 3.0 keV range into 0.1 keV energy bands. In Table 1, we provide the total number of source and background events for each energy band. Using these net counts, we generated pulse profiles, each containing 32 phases. Several example pulse profiles are shown in Figure 1.

We then calculated the discrete Fourier transforms (FFTs) of each pulse profile, using the *numpy.fft* algorithm (Harris et al. 2020). We evaluated the amplitudes of each Fourier component as $(A_n^2 + B_n^2)^{1/2}$ and of the Poisson noise using equation (A6) of Psaltis et al. (2014). In Figure 1, we show the measured Fourier amplitudes and the Poisson noise for a selected group of energy bands (see also Appendix A for details). We adopt a measurement threshold of three times the Poisson noise for each energy band and count the number of Fourier components with amplitudes larger than this threshold. We find that at most 2 components can be measured in each energy band.

Figure 2 shows the individual amplitudes of the cosine (top panel) and sine (bottom panel) Fourier components

¹ <https://zenodo.org/records/13766753>

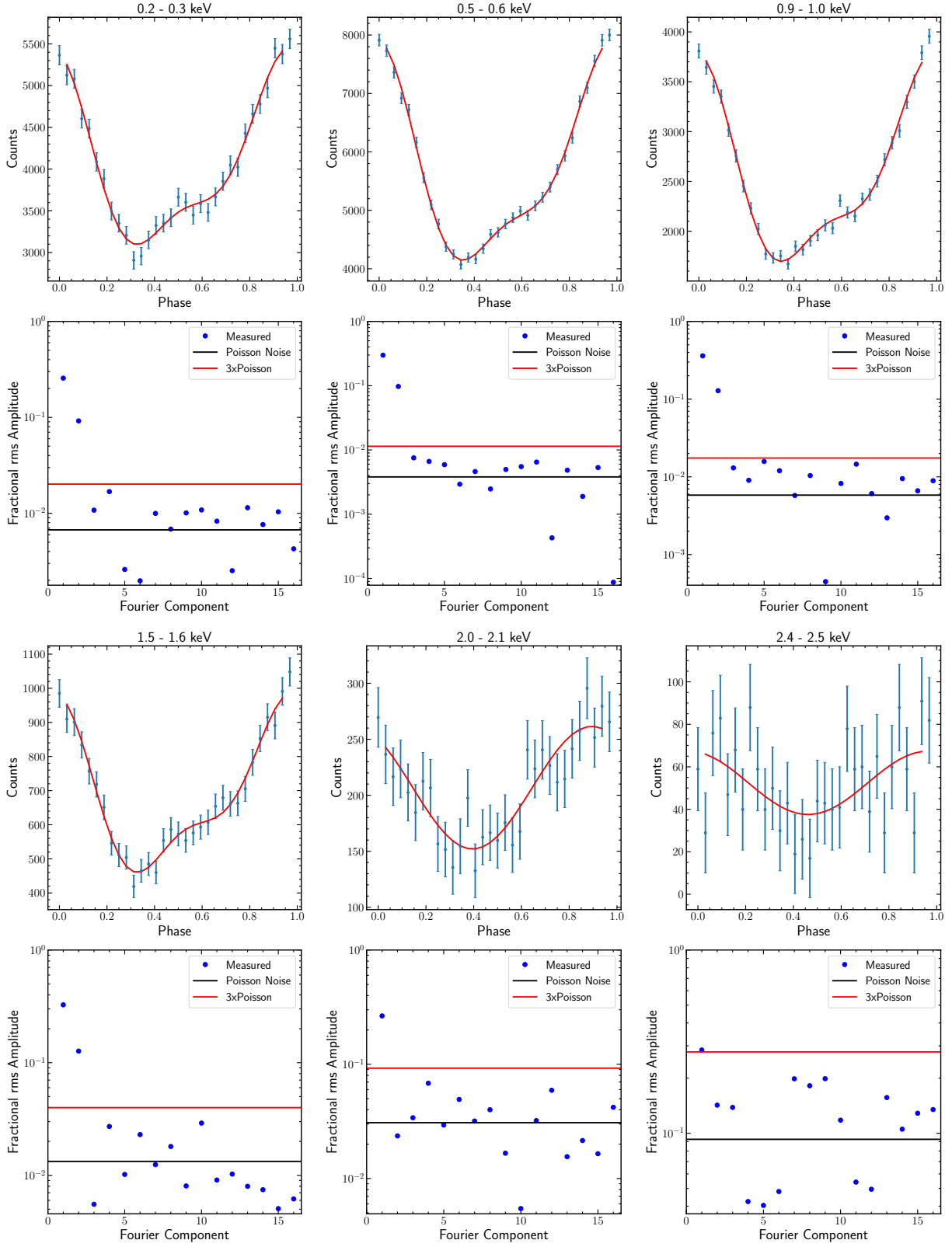


Figure 1. Pulse profiles (first and third rows) and measured amplitudes of the Fourier components (second and fourth rows) in a sample of energy bands for PSR J0437-4715. The horizontal black lines show the expected amplitude of the Poisson noise, while the red lines show our detection threshold of three times the Poisson noise. At most two Fourier components are measurable above the noise in each of the energy bands.

Table 1. Observed Counts and Backgrounds for PSR J0437–4715

Energy Range (keV)	Tot. Events ¹	Bkg. Counts ²	Net Counts ¹
0.3–0.4	303958	62858	241100
0.4–0.5	287740	58936	228804
0.5–0.6	243134	59758	183376
0.6–0.7	197956	47579	150377
0.7–0.8	165169	39835	125334
0.8–0.9	138230	36038	102192
0.9–1.0	114619	32341	82278
1.0–1.1	104235	31347	72888
1.1–1.2	71086	22896	48190
1.2–1.3	67159	24005	43154
1.3–1.4	57892	22379	35513
1.4–1.5	51396	22975	28421
1.5–1.6	42896	20865	22031
1.6–1.7	36301	18833	17468
1.7–1.8	33078	18519	14559
1.8–1.9	27596	16574	11022
1.9–2.0	23091	15080	8011
2.0–2.1	20775	14158	6617
2.1–2.2	20049	14746	5303
2.2–2.3	13169	10521	2648
2.3–2.4	12557	10881	1676
2.4–2.5	12081	10403	1678
2.5–2.6	11474	9716	1758
2.6–2.7	10778	9733	1045
2.7–2.8	10033	9062	971
2.8–2.9	9731	8970	761
2.9–3.0	9515	8668	847

¹ Total number of events within each energy band.

² Rounded total number of background events within each energy band.

as a function of photon energy, i.e., $A_n(E)$ and $B_n(E)$, for $n = 1, 2$. We see a weak energy dependence in the amplitude of the first cosine Fourier component and negligible ones in all the other components up to ~ 1.7 keV. This weak dependence significantly reduces the number of independent model parameters one can infer using the energy dependence of the pulse amplitudes, as we will discuss in §5. In addition, it is notable that above ~ 1.7 keV, the first sine component changes sign. We will show in §4 that this is related to the increasing contribution of the magnetospheric power-law component around this energy.

4. X-RAY SPECTRAL ANALYSIS

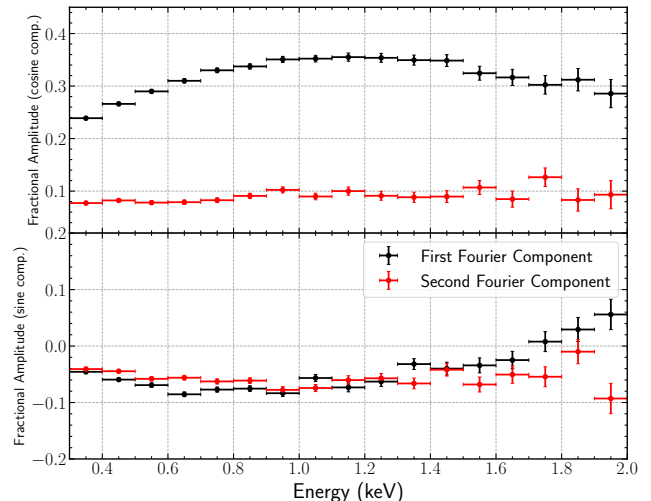


Figure 2. Amplitudes of the first two cosine (upper panel) and sine (lower panel) Fourier components as a function of energy for PSR J0437–4715. The weak dependence of these amplitudes on energy significantly reduces the number of independent model parameters that can be inferred from pulse profile modeling.

In this section, we perform a spectral analysis of PSR J0437–4715 using the longest *XMM-Newton* observations. Our main goal with this analysis is to (i) obtain flux ratios of the model components as a function of energy and (ii) show the sensitivity of these flux ratios on the assumptions and parameter uncertainties of the spectral model.

For this analysis, we used the *XMM-Newton* observation of PSR J0437–4715 (OBSID: 0603460101) and extracted MOS1 and MOS2 spectra. Note that, during the same observation, EPIC-pn data were obtained in timing mode. However, because the high background of this mode prevents any meaningful spectral analysis, we neglected this data set. For calibration, we used *emproc* within XMMAS, version 20230412_1735-21.0.0, and the latest available calibration files as of January 2025. We used circular regions centered around the source to extract the source spectrum, and nearby similar-sized regions to extract background spectra. We also used the *rmfgen* and *arfgen* tools to generate response and ancillary response matrix files, respectively. Finally, we grouped the energy bins to contain at least 150 counts per energy channel.

Following Guillot et al. (2016), we fit the X-ray spectrum of PSR J0437–4715 using a combination of three absorbed blackbodies plus a power-law component. Since the *XMM-Newton* data only allow us to fit the 0.1 – 5.0 keV range, we fix the photon index of the power-law component to $\Gamma = 1.65 \pm 0.15$ and its normalization to $(2.1_{-0.44}^{+0.56}) \times 10^{-5}$ photons/keV/cm²/s

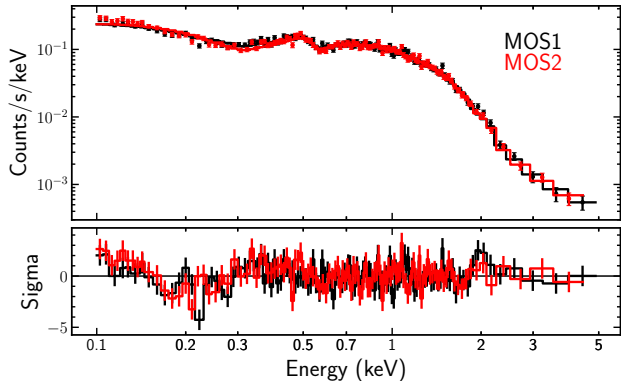


Figure 3. X-ray spectra of PSR J0437–4715, obtained with *XMM-Newton* MOS1 (black) and MOS2 (red) together with the best fit model that contains three blackbodies plus a power-law component, all absorbed due to ISM. The model parameters are from a simultaneous fit to ROSAT, *XMM-Newton* and *NuSTAR* data (Guillot et al. 2016).

at 1 keV based on the *NuSTAR* data analysis by Guillot et al. (2016). We show the MOS1 and MOS2 data, the best-fit spectral model from Guillot et al. (2016), and the residuals in Figure 3. We note that X-ray data alone cannot constrain the hydrogen column density to PSR J0437–4715, which plays a significant role in determining the relative contributions of the surface components below ~ 0.4 keV.

A large number of studies report different N_{H} values. For example, Reardon et al. (2024) find $0.8 \times 10^{20} \text{ cm}^{-2}$. The HEASARC NH Tool² gives $0.2 \times 10^{20} \text{ cm}^{-2}$ based on neutral Hydrogen observations (HI4PI Collaboration et al. 2016). González-Caniulef et al. (2019) report $0.7 - 2.4 \times 10^{20} \text{ cm}^{-2}$ using UV and soft X-ray data. Finally, Guillot et al. (2016) infer $N_{\text{H}} = 2.4 \times 10^{20} \text{ cm}^{-2}$ from their joint fit to *XMM-Newton*, ROSAT, and *NuSTAR* data. In contrast, Choudhury et al. (2024) find a value of $0.05 \times 10^{20} \text{ cm}^{-2}$ based on *NICER* observations, which is an order of magnitude smaller than any of the previously reported values.

To show the effect of the hydrogen column density value on the inferred spectral parameters, we fixed it to a sample of values covering the full range reported above, and kept the parameters of the power-law component fixed. As expected, using different values for N_{H} resulted in significant changes in the temperatures and normalizations of the thermal components. In Figure 4, we show the relative contributions of the individual spectral components to the total flux as a function

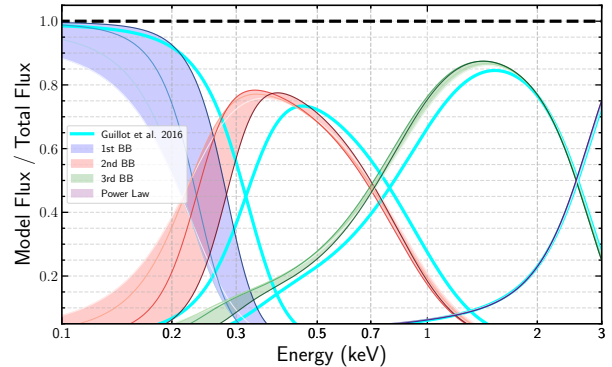


Figure 4. Fractional contribution to the total flux of each model component as a function of energy. The bands correspond to varying the hydrogen column density within the range reported in the literature. The cyan curve shows the best-fit result from Guillot et al. (2016).

of energy, with the band corresponding to the range of N_{H} values. In the same plot, we also show the best-fit model of Guillot et al. (2016). It is clear that the relative contributions of the coolest two blackbody components depend strongly on the assumed N_{H} value and vary by approximately 10% at energies less than ~ 1 keV and by as much as 50% at energies less than ~ 0.3 keV.

5. PARAMETER INFERENCE FROM COMBINED FOURIER AND SPECTRAL ANALYSES

In §3, we determined that *NICER* data of PSR J0437–4715 support the measurement of at most two Fourier components in each photon energy band, i.e., $N_{\text{max}} = 2$. In §4, we confirmed that the same data also require 3 surface emission components (blackbodies) and a magnetospheric power-law component, i.e., $S = 4$. In this section, we analyze the energy dependence of the Fourier amplitudes that correspond to each spectral component in order to quantify the total number of independent parameters that can be inferred from the combined Fourier and spectral information. This will inform the maximum complexity of any model of the surface emission that can be robustly constrained by the data.

We first write the energy dependence of the fractional Fourier amplitude of each spectral component as a polynomial in E , i.e.,

$$\frac{A_{in}(E)}{A_{i0}(E)} = \left[f_{in} + f'_{in}E + \frac{1}{2}f''_{in}E^2 + \dots \right]. \quad (8)$$

We then determine the number of terms in this expansion that are necessary to reproduce the observational data. We will show that each component requires only the constant term. In other words, the pulse fraction of each spectral component does not evolve as a func-

² <https://heasarc.gsfc.nasa.gov/cgi-bin/Tools/w3nh/w3nh.pl>

tion of energy, within the uncertainties of the current measurements.

To demonstrate this, we rewrite equations (5)-(7) as

$$\frac{A_n(E)}{A_0(E)} = \sum_{i=1}^4 f_{in} \left[\frac{A_{i0}(E)}{A_0(E)} \right] \cos(n\phi_{in}) \quad (9)$$

$$\frac{B_n(E)}{A_0(E)} = \sum_{i=1}^4 f_{in} \left[\frac{A_{i0}(E)}{A_0(E)} \right] \sin(n\phi_{in}), \quad (10)$$

where $A_n(E)/A_0(E)$ and $B_n(E)/A_0(E)$ are the fractional cosine and sine amplitudes shown in Figure 2 and $A_{i0}(E)/A_0(E)$ are the fractional contributions to the total flux of each spectral component shown in Figure 4. Note that, for each surface component, the angular arguments ϕ_{in} are determined only by the azimuth of the hotspot associated with that spectral component on the neutron star surface. As such, ϕ_{in} should not depend on n . However, this is not necessarily true for the magnetospheric power-law component. When fitting the data, we will allow for these angular arguments to depend on n even for the thermal components and show that they are consistent with being constant between the various Fourier components.

We obtain the parameters f_{in} and ϕ_{in} by fitting equations (9)-(10) to the Fourier components we measured in §3, using the fractional flux contributions of the spectral components we inferred in §4. We only use data up to 2 keV, beyond which the spectra are dominated by the magnetospheric power-law component. We account for the uncertainty introduced by N_H on the fractional flux contributions of the spectral components by adding a 5% systematic uncertainty (see Fig. 4) to the measurements.

In order to quantify the posteriors and explore the correlations between the inferred parameters, we employed a modified version of the Markov Chain Monte Carlo algorithm MARCH (MARKov Chains for HORIZONS, Psaltis et al. 2022). Originally developed for fitting interferometric data from the Event Horizon Telescope, MARCH, uses parallel tempering and is optimized for high performance.

Figure 5 combines the information from Figures 2 and 4 and also shows the inferred best-fit model (eqs.[9]-[10]) that connects them. Clearly, the observed weak energy dependence of the various Fourier components can be accounted for by simply assuming that the fractional pulse profile of each spectral component does not depend on energy. Moreover, the sign change of the fundamental component of the sine Fourier series at energy ~ 1.7 keV clearly follows the increase in the flux contribution of the power-law component, which shows substantial pulsations.

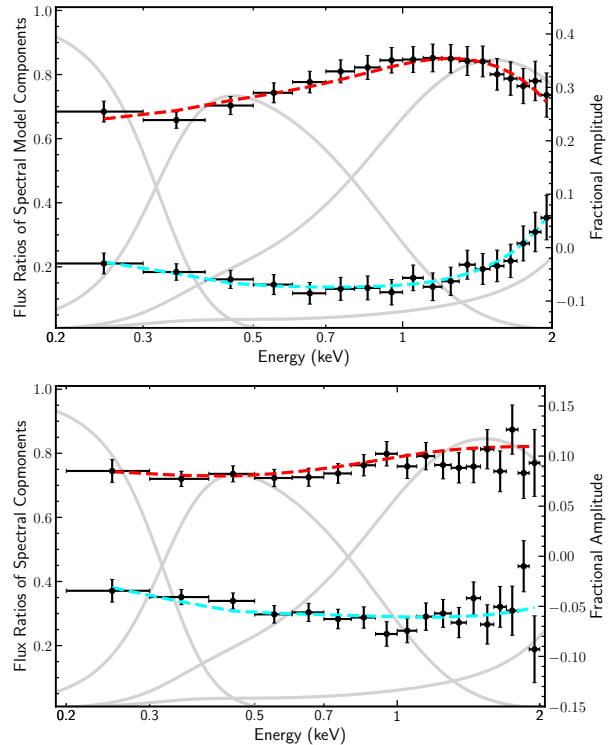


Figure 5. Grey curves show the fractional flux contributions of the four spectral components (see Fig. 4). Error bars show the fractional amplitudes of the fundamental (upper panel) and harmonic (lower panel) cosine and sine components of the pulse profiles (see Fig. 2). The dashed lines show the predicted fractional amplitudes for the model described in the text.

Figure 6 shows the resulting posteriors for the parameters $f_1 - f_4$ and $\phi_1 - \phi_4$ for $n = 1, 2$. Table 2 contains the best-fit parameters together with their 68% credible intervals. As expected, the angular arguments ϕ_{in} of the surface spectral components do not depend on the harmonic number, i.e., the blue and red contours for $\phi_1 - \phi_3$ overlap. However, this is not true for the power-law component, which is thought to be of magnetospheric origin. Interestingly, the inferred azimuths of the three spectral components ϕ_1, ϕ_2 , and ϕ_3 are very close to each other; suggesting that these surface components are nearly collocated. Table 2 allows us to count the maximum number of independent parameters that can be inferred from the current *NICER* data for this source. For each surface spectral component, we can measure the temperature and radius of the emitting region from the DC component, the amplitudes of the fundamental and harmonic Fourier components, and their common phase. As a result, the total number of theoretical model parameters of surface emission that can be used to model PSR J0437-4715 cannot exceed 15. In the next section, we will discuss the broader implications of this result

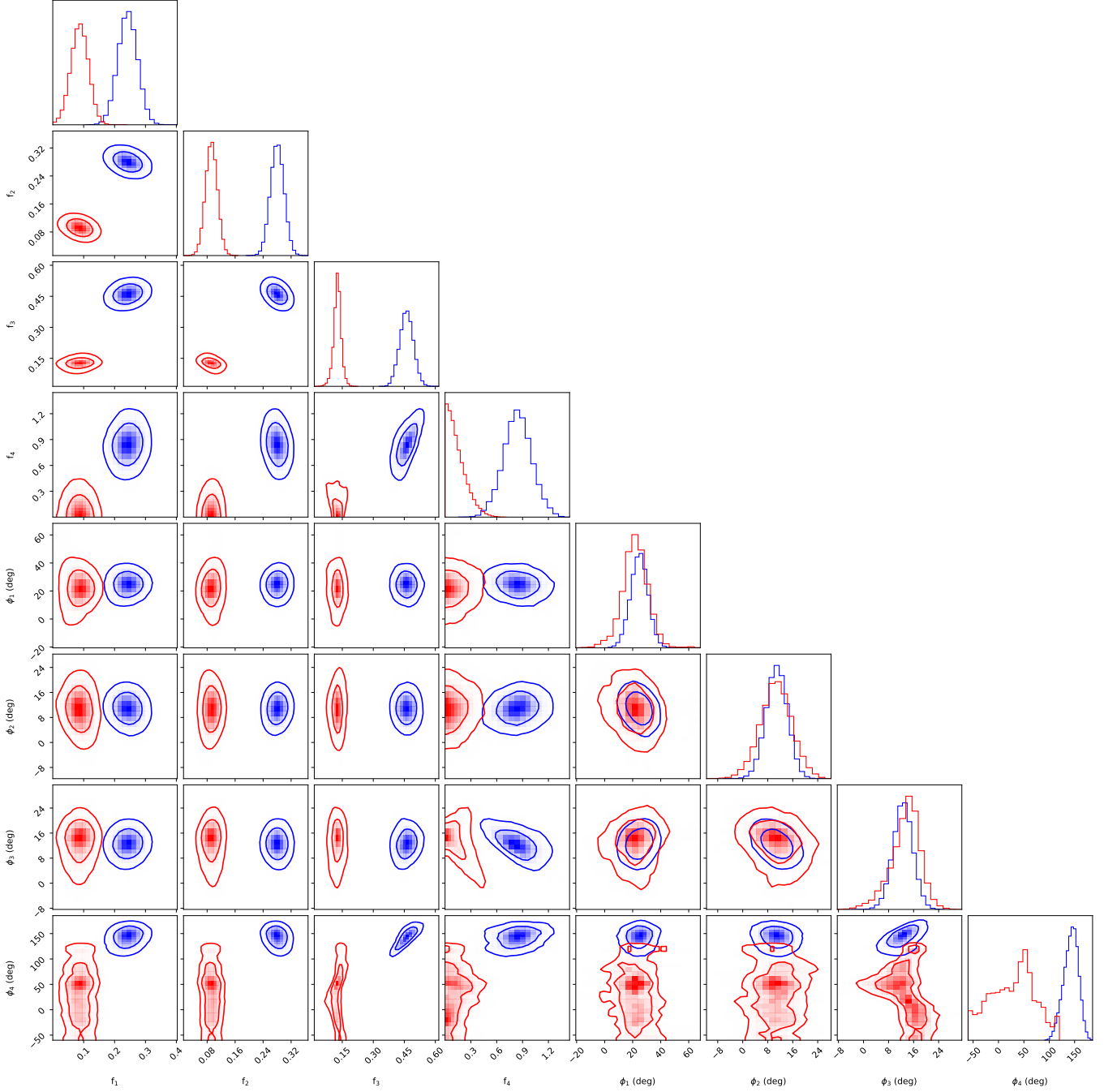


Figure 6. The posteriors of the fractional Fourier amplitudes f_{in} and angular arguments ϕ_{in} of the four spectral components in PSR J0437–4715. Blue curves correspond to the fundamental components ($n = 1$) and red curves to the harmonics ($n = 2$).

for model fitting and parameter inference from *NICER* pulse profiles.

6. CONCLUSIONS

We investigated the relation between the amplitudes of the Fourier components of pulse profiles of PSR J0437–4715 and the X-ray spectral components using *NICER* and *XMM-Newton* data. We found that the

Fourier decomposition of the pulse profiles at different energies supports the detection of two Fourier components that are statistically significant. By combining this information with the X-ray spectral data, we determined that at most 15 independent model parameters can be inferred from the combined timing and spectral data from this source. Equally importantly, we determined that the power-law component of the spectrum,

Table 2. Spectral components and their corresponding contributions to Fourier amplitudes

Spectral Component	Parameters ¹ kT (eV), R (km)	Fundamental		Harmonic	
		Amplitude	Phase	Amplitude	Phase
		f_{i1}	ϕ_{i1} (deg)	f_{i2}	ϕ_{i2} (deg)
Blackbody 1	32, 10.98	0.24 ± 0.03	$24.74^{+6.02}_{-6.26}$	0.09 ± 0.03	$21.82^{+8.55}_{-8.43}$
Blackbody 2	125, 0.25	0.28 ± 0.02	$10.91^{+3.39}_{-3.43}$	0.09 ± 0.02	$10.69^{+4.88}_{-5.00}$
Blackbody 3	271, 0.04	0.46 ± 0.03	$12.61^{+3.10}_{-3.17}$	0.13 ± 0.02	$13.94^{+5.16}_{-3.75}$
Power-law	$\Gamma=1.65, 2.1 \times 10^{-5}$	0.84 ± 0.16	$143.73^{+13.20}_{-15.87}$	$0.11^{+0.14}_{-0.08}$	$33.92^{+38.12}_{-53.87}$

¹ Values are adopted from [Guillot et al. \(2016\)](#).

which is presumed to be of magnetospheric origin, shows substantial pulsations with significant harmonic structure.

We generalized our analyses to the three additional sources for which *NICER* carried out sustained observing campaigns for pulse profile modeling. We show the results in Appendix B. For PSR J0030+0451, we can also detect up to two Fourier components, but only at energies $E \lesssim 2$ keV. For this source, the first harmonic is stronger than the fundamental, which is consistent with the high inferred inclination. The spectrum of this source, however, shows evidence for a single blackbody and a power law component, with the blackbody making at most a comparable contribution as the power law in the 0.6 – 1.3 keV range, and being subdominant everywhere else. Adopting an alternative model with only blackbody components results in a fit that is statistically worse. More importantly, that model leads to an unphysically low value for the interstellar extinction, forcing the hydrogen column density to become practically zero. This is probably similar to the extremely low value of the hydrogen column density inferred for PSR J0437–4715 by [Choudhury et al. \(2024\)](#) that is inconsistent with those of alternative measurements.

For PSR J0740+6620, it is barely possible to detect 1 or 2 Fourier components for $0.3 \leq E \leq 1$ keV, at marginal statistical significance. For this reason, we did not perform a spectral analysis for this source.

Finally, for PSR J1231–1411, up to three Fourier components can be detected for energies up to ~ 1.3 keV, beyond which there are no detectable source counts above the background. The X-ray spectrum of this source is dominated by a power law at all photon energies: it has a factor of 5 higher contribution than the blackbody at 0.3 keV and 50% more contribution at 1 keV.

There are two conclusions that can be reached from this broader analysis. The first relates to the treatment of the power-law component. In previous studies of *NICER* targets, the presence of the power-law component has either been neglected or has been incorporated as an unmodulated component of the background ([Riley et al. 2019](#); [Choudhury et al. 2024](#)). In PSR J0437–4715,

[Guillot et al. \(2016\)](#) demonstrated conclusively that the power-law component shows significant pulsations. Our analysis here confirms and, in fact, requires the presence of pulsations in the power-law component, even at energies as low as 1 keV. This invalidates the assumption in the previous studies and is likely to change the resulting values for the neutron-star radius for this source, and possibly also for the sources discussed in the Appendix.

The second conclusion is related to the information content of the pulse profiles and spectra and the number of parameters that can be robustly inferred from theoretical modeling. *Each* thermal surface component included in pulse-profile models requires a minimum of 4 parameters, which are the size, temperature, and the two position angles of the hotspot on the stellar surface, assuming the simplest case of a circular, uniform-temperature spot. In addition, the neutron star introduces two baseline parameters, which are its compactness and the observer’s inclination with respect to its spin axis, without counting the distance and hydrogen column density to the source or the beaming pattern of radiation from the surface, all of which are assumed to be known or modeled independently.

On the measurement side, our analysis has shown that each spectral component typically provides 5 constraints: the flux and temperature of each surface component as well as two amplitudes and 1 phase angle from the Fourier analysis of the pulse profiles. This means that, with the present quality of the data, sources that show one thermal spectral component do not provide sufficient information to infer surface emission and neutron star parameters, even when adopting the simplest model for that emission and neglecting all other assumptions and uncertainties. For a source with three spectral components, such as PSR J0437–4715, which provides 15 measurable quantities, there is sufficient information to infer both the parameters of three simple hotspots as well as of the neutron star, which require 14 parameters to describe. However, the beaming of radiation, the column density and distance, as well as the presence of the pulsed power-law component can add significant

systematic uncertainties and biases that may be difficult to account for.

One final point to discuss is the advantage of using data from multiple observatories in combined pulse profile and spectral modeling, and the resulting parameter inference. With its precise timing capabilities and larger effective area, *NICER* XTI is an excellent instrument for studying energy-dependent pulse profiles of nearby pulsars that show thermal components in their spectra. However, its non-imaging nature and the relatively low count rates of the target pulsars result in non-negligible and time varying contribution from various background sources. Choudhury et al. (2024), who studied the effects of background and used *XMM-Newton* data for cross-checking, found that the background emission estimated using the 3C50 background model (Remillard et al. 2022) becomes comparable to source counts at ~ 1.5 keV, as well as below 0.3 keV (see also Table 1). We note that these limits also coincide with the energy range where a non-thermal component becomes easily detectable (in the higher energies) and a larger but cooler blackbody emission becomes dominant (in the low energies, see Figure 4).

Similar issues are also visible in the energy-dependent pulse profiles shown in Appendix Appendix B for the other pulsars, PSR J0030+0451, PSR J1231-1411, PSR J0740+6620. *XMM-Newton*, in contrast, provides significantly more reliable phase-averaged spectral data, owing to its much lower background and broader spectral sensitivity. Therefore, obtaining the spectral components from the *XMM-Newton* data and using their fractional contribution to the total emission, under the assumption that these components do not show significant changes within the *NICER* observations used here, is likely to lead to smaller uncertainties than using *NICER* data alone.

ACKNOWLEDGEMENTS

T.G. greatly appreciates the hospitality at the School of Physics at the Georgia Institute of Technology, where this work was completed.

DATA AVAILABILITY

All the data used in this paper are publicly available through the NASA/HEASARC archives. The data from Choudhury et al. (2024) is available through Zenodo services.

REFERENCES

- Bauböck, M., Psaltis, D., & Özel, F. 2019, *The Astrophysical Journal*, 872, 162, doi: [10.3847/1538-4357/aaf08](https://doi.org/10.3847/1538-4357/aaf08)
- Becker, W., & Trümper, J. 1993, *Nature*, 365, 528, doi: [10.1038/365528a0](https://doi.org/10.1038/365528a0)
- Bogdanov, S. 2013, *ApJ*, 762, 96, doi: [10.1088/0004-637X/762/2/96](https://doi.org/10.1088/0004-637X/762/2/96)
- Bogdanov, S., & Grindlay, J. E. 2009, *ApJ*, 703, 1557, doi: [10.1088/0004-637X/703/2/1557](https://doi.org/10.1088/0004-637X/703/2/1557)
- Bogdanov, S., Grindlay, J. E., & Rybicki, G. B. 2008, *ApJ*, 689, 407, doi: [10.1086/592341](https://doi.org/10.1086/592341)
- Bogdanov, S., Heinke, C. O., Özel, F., & Güver, T. 2016, *ApJ*, 831, 184, doi: [10.3847/0004-637X/831/2/184](https://doi.org/10.3847/0004-637X/831/2/184)
- Bogdanov, S., Rybicki, G. B., & Grindlay, J. E. 2007, *ApJ*, 670, 668, doi: [10.1086/520793](https://doi.org/10.1086/520793)
- Boztepe, T., Gögüş, E., Güver, T., & Schwenzer, K. 2020, *MNRAS*, 498, 2734, doi: [10.1093/mnras/staa2503](https://doi.org/10.1093/mnras/staa2503)
- Brambilla, G., Kalapotharakos, C., Timokhin, A. N., Harding, A. K., & Kazanas, D. 2018, *ApJ*, 858, 81, doi: [10.3847/1538-4357/aab3e1](https://doi.org/10.3847/1538-4357/aab3e1)
- Choudhury, D., Salmi, T., Vinciguerra, S., et al. 2024, *The Astrophysical Journal Letters*, 971, L20, doi: [10.3847/2041-8213/ad5a6f](https://doi.org/10.3847/2041-8213/ad5a6f)
- Damen, E., Magnier, E., Lewin, W. H. G., et al. 1990, *A&A*, 237, 103
- Dittmann, A. J., Miller, M. C., Lamb, F. K., et al. 2024, *The Astrophysical Journal*, 974, 295, doi: [10.3847/1538-4357/ad5fle](https://doi.org/10.3847/1538-4357/ad5fle)
- Echiburú, C. S., Guillot, S., Zhao, Y., et al. 2020, *MNRAS*, 495, 4508, doi: [10.1093/mnras/staa1456](https://doi.org/10.1093/mnras/staa1456)
- Gendreau, K. C., Arzoumanian, Z., & Okajima, T. 2012, in *Society of Photo-Optical Instrumentation Engineers (SPIE) Conference Series*, Vol. 8443, *Space Telescopes and Instrumentation 2012: Ultraviolet to Gamma Ray*, ed. T. Takahashi, S. S. Murray, & J.-W. A. den Herder, 844313, doi: [10.1117/12.926396](https://doi.org/10.1117/12.926396)
- González-Caniulef, D., Guillot, S., & Reisenegger, A. 2019, *MNRAS*, 490, 5848, doi: [10.1093/mnras/stz2941](https://doi.org/10.1093/mnras/stz2941)
- Guillot, S., Kaspi, V. M., Archibald, R. F., et al. 2016, *MNRAS*, 463, 2612, doi: [10.1093/mnras/stw2194](https://doi.org/10.1093/mnras/stw2194)
- Güver, T., Özel, F., Cabrera-Lavers, A., & Wroblewski, P. 2010a, *ApJ*, 712, 964, doi: [10.1088/0004-637X/712/2/964](https://doi.org/10.1088/0004-637X/712/2/964)
- Güver, T., Wroblewski, P., Camarota, L., & Özel, F. 2010b, *ApJ*, 719, 1807, doi: [10.1088/0004-637X/719/2/1807](https://doi.org/10.1088/0004-637X/719/2/1807)
- Harris, C. R., Millman, K. J., van der Walt, S. J., et al. 2020, *Nature*, 585, 357, doi: [10.1038/s41586-020-2649-2](https://doi.org/10.1038/s41586-020-2649-2)

- Heinke, C. O., Cohn, H. N., Lugger, P. M., et al. 2014, *MNRAS*, 444, 443, doi: [10.1093/mnras/stu1449](https://doi.org/10.1093/mnras/stu1449)
- HI4PI Collaboration, Ben Bekhti, N., Flöer, L., et al. 2016, *A&A*, 594, A116, doi: [10.1051/0004-6361/201629178](https://doi.org/10.1051/0004-6361/201629178)
- Johnston, S., Lorimer, D. R., Harrison, P. A., et al. 1993, *Nature*, 361, 613, doi: [10.1038/361613a0](https://doi.org/10.1038/361613a0)
- Lattimer, J. M., & Prakash, M. 2001, *ApJ*, 550, 426, doi: [10.1086/319702](https://doi.org/10.1086/319702)
- Lewin, W. H. G., van Paradijs, J., & Taam, R. E. 1993, *SSRv*, 62, 223, doi: [10.1007/BF00196124](https://doi.org/10.1007/BF00196124)
- Lorimer, D. R. 2008, *Living Reviews in Relativity*, 11, 8, doi: [10.12942/lrr-2008-8](https://doi.org/10.12942/lrr-2008-8)
- Miller, M. C., Lamb, F. K., Dittmann, A. J., et al. 2019, *The Astrophysical Journal Letters*, 887, L24, doi: [10.3847/2041-8213/ab50c5](https://doi.org/10.3847/2041-8213/ab50c5)
- Morsink, S. M., & Leahy, D. A. 2011, *ApJ*, 726, 56, doi: [10.1088/0004-637X/726/1/56](https://doi.org/10.1088/0004-637X/726/1/56)
- Oppenheimer, J. R., & Volkoff, G. M. 1939, *Phys. Rev.*, 55, 374, doi: [10.1103/PhysRev.55.374](https://doi.org/10.1103/PhysRev.55.374)
- Özel, F. 2013, *Reports on Progress in Physics*, 76, 016901, doi: [10.1088/0034-4885/76/1/016901](https://doi.org/10.1088/0034-4885/76/1/016901)
- Özel, F., Baym, G., & Güver, T. 2010, *PhRvD*, 82, 101301, doi: [10.1103/PhysRevD.82.101301](https://doi.org/10.1103/PhysRevD.82.101301)
- Özel, F., & Freire, P. 2016, *ARA&A*, 54, 401, doi: [10.1146/annurev-astro-081915-023322](https://doi.org/10.1146/annurev-astro-081915-023322)
- Özel, F., Psaltis, D., Güver, T., et al. 2016, *ApJ*, 820, 28, doi: [10.3847/0004-637X/820/1/28](https://doi.org/10.3847/0004-637X/820/1/28)
- Paradijs, J. v. 1978, *Nature*, 274, 650, doi: [10.1038/274650a0](https://doi.org/10.1038/274650a0)
- Paradijs, J. v., & Lewin, W. H. G. 1978, *Nature*, 276, 249, doi: [10.1038/276249a0](https://doi.org/10.1038/276249a0)
- Paradijs, J. v., & Lewin, W. H. G. 1993, *Classical and Quantum Gravity*, 10, S117, doi: [10.1088/0264-9381/10/s/012](https://doi.org/10.1088/0264-9381/10/s/012)
- Pechenick, K. R., Ftaclas, C., & Cohen, J. M. 1983, *The Astrophysical Journal*, 274, 846, doi: [10.1086/161498](https://doi.org/10.1086/161498)
- Pechenick, K. R., Ftaclas, C., & Cohen, J. M. 1983, *ApJ*, 274, 846, doi: [10.1086/161498](https://doi.org/10.1086/161498)
- Philippov, A. A., Spitkovsky, A., & Cerutti, B. 2015, *ApJL*, 801, L19, doi: [10.1088/2041-8205/801/1/L19](https://doi.org/10.1088/2041-8205/801/1/L19)
- Poutanen, J., & Beloborodov, A. M. 2006, *Monthly Notices of the Royal Astronomical Society*, 373, 836, doi: [10.1111/j.1365-2966.2006.11088.x](https://doi.org/10.1111/j.1365-2966.2006.11088.x)
- Psaltis, D., & Özel, F. 2014, *ApJ*, 792, 87, doi: [10.1088/0004-637X/792/2/87](https://doi.org/10.1088/0004-637X/792/2/87)
- Psaltis, D., Özel, F., & Chakrabarty, D. 2014, *The Astrophysical Journal*, 787, 136, doi: [10.1088/0004-637x/787/2/136](https://doi.org/10.1088/0004-637x/787/2/136)
- Psaltis, D., Özel, F., Medeiros, L., et al. 2022, *ApJ*, 928, 55, doi: [10.3847/1538-4357/ac2c69](https://doi.org/10.3847/1538-4357/ac2c69)
- Reardon, D. J., Bailes, M., Shannon, R. M., et al. 2024, *ApJL*, 971, L18, doi: [10.3847/2041-8213/ad614a](https://doi.org/10.3847/2041-8213/ad614a)
- Remillard, R. A., Loewenstein, M., Steiner, J. F., et al. 2022, *AJ*, 163, 130, doi: [10.3847/1538-3881/ac4ae6](https://doi.org/10.3847/1538-3881/ac4ae6)
- Riley, T. E., Watts, A. L., Bogdanov, S., et al. 2019, *The Astrophysical Journal Letters*, 887, L21, doi: [10.3847/2041-8213/ab481c](https://doi.org/10.3847/2041-8213/ab481c)
- Riley, T. E., Watts, A. L., Ray, P. S., et al. 2021, *The Astrophysical Journal Letters*, 918, L27, doi: [10.3847/2041-8213/ac0a81](https://doi.org/10.3847/2041-8213/ac0a81)
- Ruderman, M. A., & Sutherland, P. G. 1975, *ApJ*, 196, 51, doi: [10.1086/153393](https://doi.org/10.1086/153393)
- Salmi, T., Deneva, J. S., Ray, P. S., et al. 2024a, *The Astrophysical Journal*, 976, 58, doi: [10.3847/1538-4357/ad81d2](https://doi.org/10.3847/1538-4357/ad81d2)
- Salmi, T., Choudhury, D., Kini, Y., et al. 2024b, *The Astrophysical Journal*, 974, 294, doi: [10.3847/1538-4357/ad5f1f](https://doi.org/10.3847/1538-4357/ad5f1f)
- Schwenzer, K., Boztepe, T., Güver, T., & Vurgun, E. 2017, *MNRAS*, 466, 2560, doi: [10.1093/mnras/stw3201](https://doi.org/10.1093/mnras/stw3201)
- Shaw, A. W., Heinke, C. O., Steiner, A. W., et al. 2018, *MNRAS*, 476, 4713, doi: [10.1093/mnras/sty582](https://doi.org/10.1093/mnras/sty582)
- Steiner, A. W., Lattimer, J. M., & Brown, E. F. 2010, *ApJ*, 722, 33, doi: [10.1088/0004-637X/722/1/33](https://doi.org/10.1088/0004-637X/722/1/33)
- . 2013, *ApJL*, 765, L5, doi: [10.1088/2041-8205/765/1/L5](https://doi.org/10.1088/2041-8205/765/1/L5)
- Tolman, R. C. 1939, *Phys. Rev.*, 55, 364, doi: [10.1103/PhysRev.55.364](https://doi.org/10.1103/PhysRev.55.364)
- van Paradijs, J. 1982, *A&A*, 107, 51
- Watts, A. L., Andersson, N., Chakrabarty, D., et al. 2016, *Reviews of Modern Physics*, 88, 021001, doi: [10.1103/RevModPhys.88.021001](https://doi.org/10.1103/RevModPhys.88.021001)
- Weinberg, N., Miller, M. C., & Lamb, D. Q. 2001, *The Astrophysical Journal*, 546, 1098, doi: [10.1086/318279](https://doi.org/10.1086/318279)
- Yao, J. M., Manchester, R. N., & Wang, N. 2017, *ApJ*, 835, 29, doi: [10.3847/1538-4357/835/1/29](https://doi.org/10.3847/1538-4357/835/1/29)
- Zavlin, V. E., & Pavlov, G. G. 2002, in *Neutron Stars, Pulsars, and Supernova Remnants*, ed. W. Becker, H. Lesch, & J. Trümper, 263, doi: [10.48550/arXiv.astro-ph/0206025](https://doi.org/10.48550/arXiv.astro-ph/0206025)
- Özel, F., Güver, T., & Psaltis, D. 2009, *The Astrophysical Journal*, 693, 1775, doi: [10.1088/0004-637x/693/2/1775](https://doi.org/10.1088/0004-637x/693/2/1775)

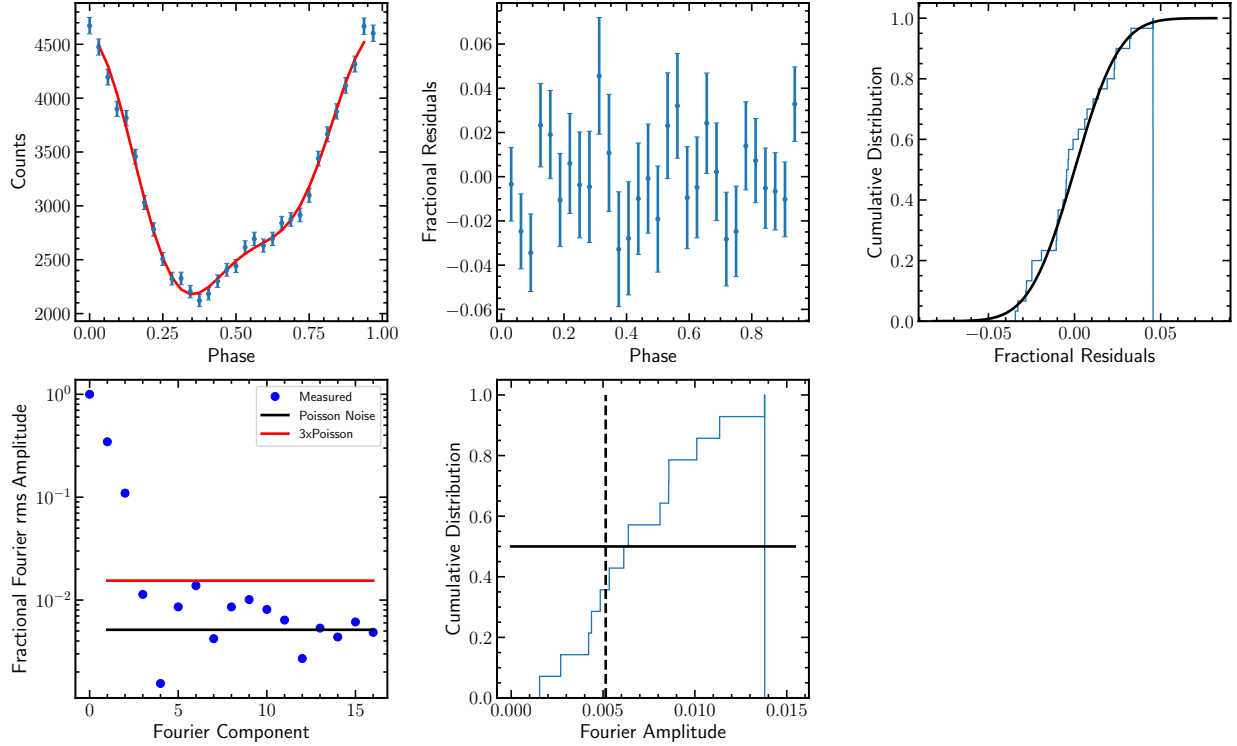


Figure A1. The 0.8–0.9 keV pulse profile of PSR J0437–4715 obtained with *NICER*, as a representative example. From upper left to lower right, the panels show: the pulse profile (blue points) and the model neglecting all Fourier components with amplitudes below 3 times the Poisson noise level (red curve); the residuals from neglecting these Fourier components, showing no systematic dependence on pulse phase; the cumulative distribution of these residuals comparing them also to the expected normal distribution (black curve); the fractional rms amplitudes of the Fourier components together with the expected level of the Poisson noise (black) and 3 times that level (red); and the cumulative distribution of the Fourier amplitudes, demonstrating that the median of this distribution (horizontal black line) closely matches the expected value.

APPENDIX

A. ADDITIONAL DETAILS OF THE FOURIER ANALYSIS

In this appendix, we provide additional details and tests of our pulse profile analysis.

In [Figure A1](#), we show the results of our detailed analysis of the pulse profiles from PSR J0437–4715, using the 0.8–0.9 keV range as a representative example. In addition to the pulse profile and the Fourier components, we also show the residuals from neglecting the Fourier components with amplitudes below 3 times the Poisson level, the cumulative distribution of these residuals, as well as the distribution of the Fourier amplitudes of the components that are within 3 times the Poisson noise level. Neglecting these Fourier components results in residuals that show no systematic dependence on pulse phase and with a distribution that closely follows the expected normal distribution. Moreover, the median of the cumulative distribution of Fourier amplitudes closely matches the expected value calculated using eq. (A6) of [Psaltis et al. \(2014\)](#). All these suggest that there is no evidence of any systematics in our analysis and that our thresholds accurately describe the noise level of the measurements.

We also test the effects of the selection of energy intervals for pulse profile analysis. Specifically, in [Fig. A2](#), we show the results of the analysis for different widths of the energy range, i.e., the effect of broadening the energy range we take into account to calculate the pulse profiles and Fourier components. For illustration, we extend the range from 0.3–0.4 keV to 0.3–0.6 keV. There is negligible effect on the number of components that are detectable and on their inferred amplitudes, for reasonable extents of the energy range, before they become wide enough to encompass different spectral components.

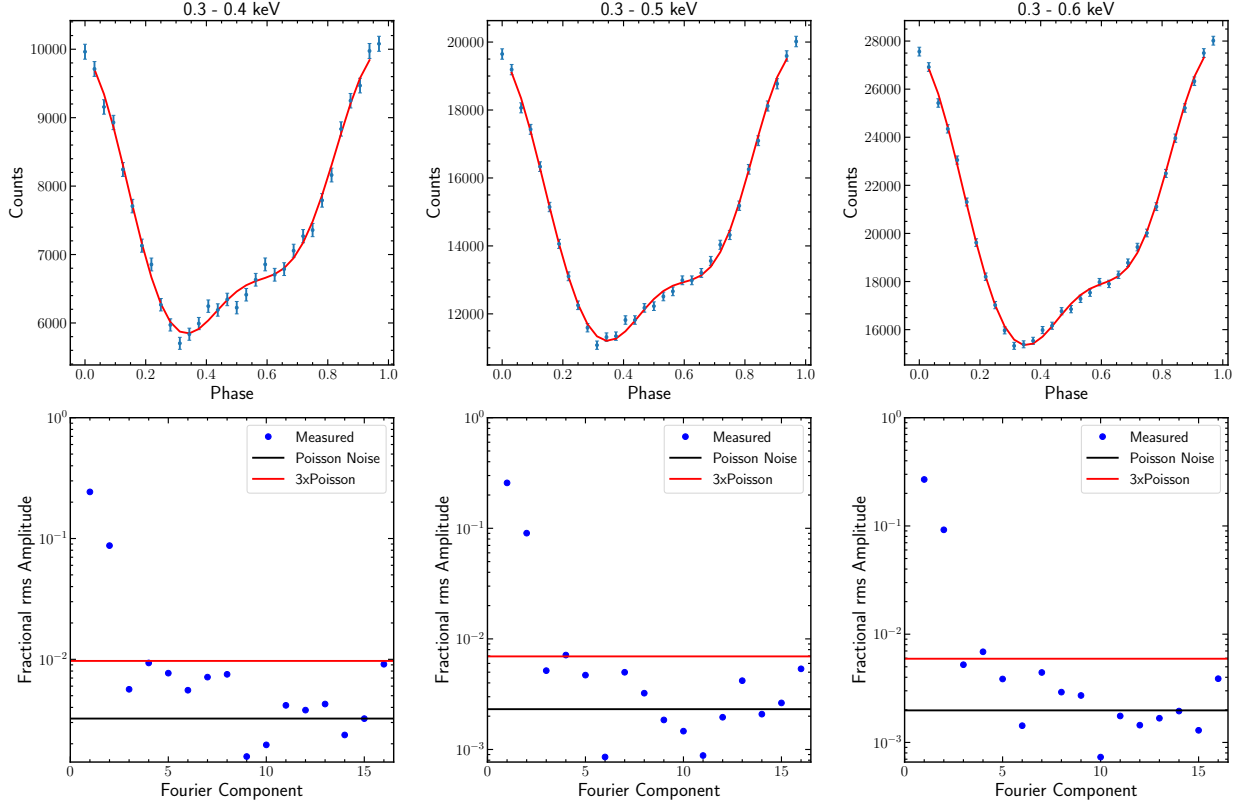


Figure A2. Same as Figure 1 but showing the effect of increasing the width of the energy range over which we perform the Fourier decomposition.

B. OTHER SOURCES

Here we present our analysis of three additional *NICER* targets, namely PSR J0030+0451, PSR J0740+6620, and PSR J1231-1411.

B.1. PSR J0030+0451

In Figure B3, we show examples of pulse profiles obtained with *NICER* at several energy bands, similar to the ones shown in Figure 1 for PSR J0437-4715. Note that we did not perform a background subtraction as no background file for *NICER* data is present in the Zenodo archives for this source. It is evident that pulsations are detectable only up to 2 keV.

We also show in Figure B4 the spectra of PSR J0030+0451 obtained with *XMM-Newton*. The spectra show evidence for only one thermal component and a significant power-law component that dominates over the thermal one at $E \lesssim 0.6$ keV and $E \gtrsim 1.3$ keV (with a χ^2 of 130.13 for 111 degrees of freedom). The X-ray spectra can also be modeled with a combination of two blackbodies, but this fit results in a worse χ^2 of 151.99 for the same degrees of freedom. However, in the latter case, the hydrogen column density attains an unphysically small value that is consistent with zero.

B.2. PSR J0740+6620

In Figure B5, we show examples of pulse profiles obtained with *NICER* at several energy bands for PSR J0740+6620. The pulsations are (marginally) detectable between 0.3 and 1 keV, with at most 2 harmonics. This source has not been detected by *XMM-Newton* and, therefore, no X-ray spectrum is shown.

B.3. PSR J1231-1411

In Figure B6, we show examples of pulse profiles obtained with *NICER* at several energy bands for PSR J1231-1411. For this pulsar, the background dominates in multiple energy bands; beyond 1.3 keV, subtraction of the background results in no net source counts. Up to three Fourier components are detectable in some of the energy bands.

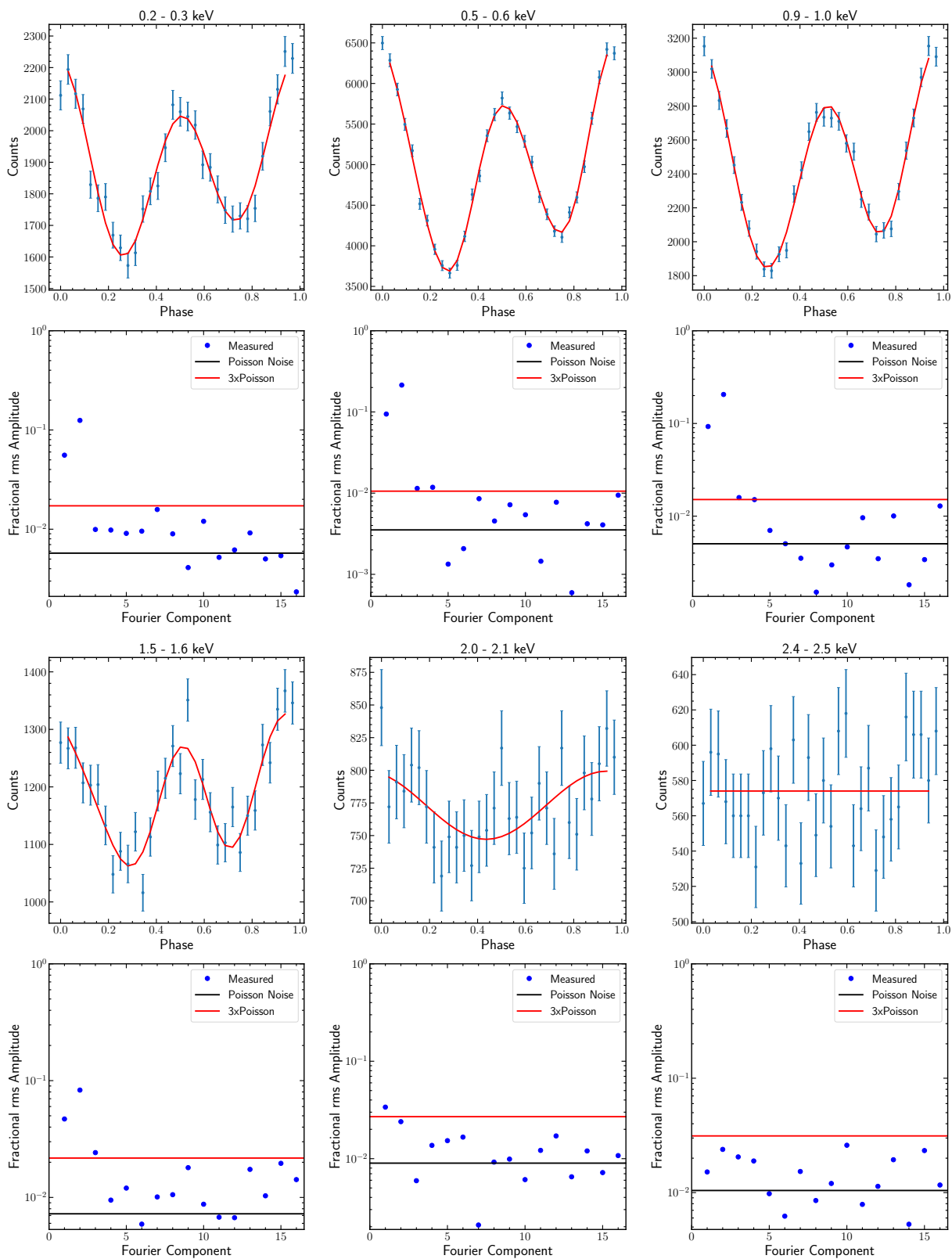


Figure B3. Same as Figure 1 but for PSR J0030+0451. Pulses are only detectable below 2.0 keV.

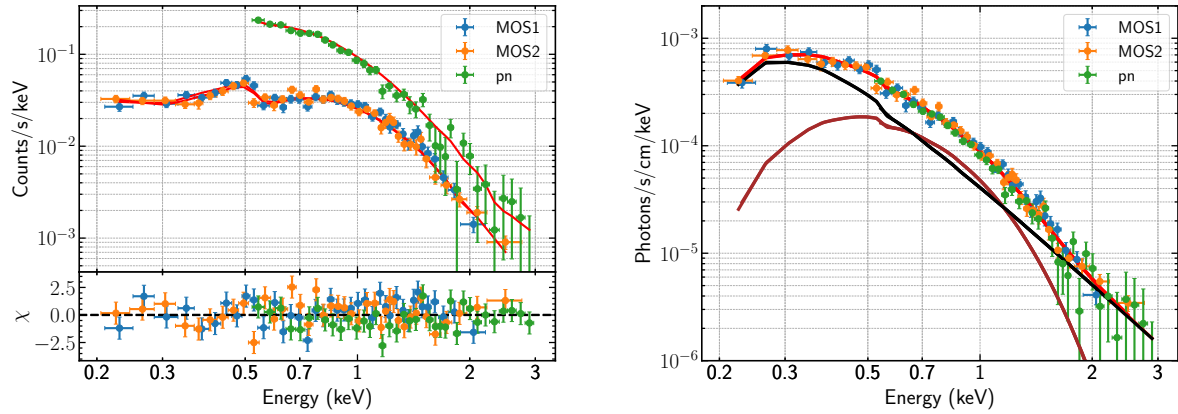


Figure B4. X-ray spectra of PSR J0030+0451 obtained with *XMM-Newton*. The left panel shows the data and the best fit model (upper panel) together with residuals (lower panel). The right panel shows the model components, which include an absorbed blackbody (red) and a power-law (black) component.

Figure B7 shows the X-ray spectrum obtained with *XMM-Newton*, as well as the best-fit model. The spectral parameters are obtained from [Schwenzer et al. \(2017\)](#) and [Boztepe et al. \(2020\)](#), which also included *Chandra* and *SUZAKU* data. The one thermal component is significantly subdominant (up to a factor of 5) to the power-law component at all energies. Because of this, it is unclear what fraction of the pulsations are attributable to the surface thermal components. Fitting this dataset with two blackbodies results in large residuals towards high energies and an apparent emitting radius for one of the thermal components that is as small as 49 m, assuming a distance of 420 pc ([Yao et al. 2017](#)).

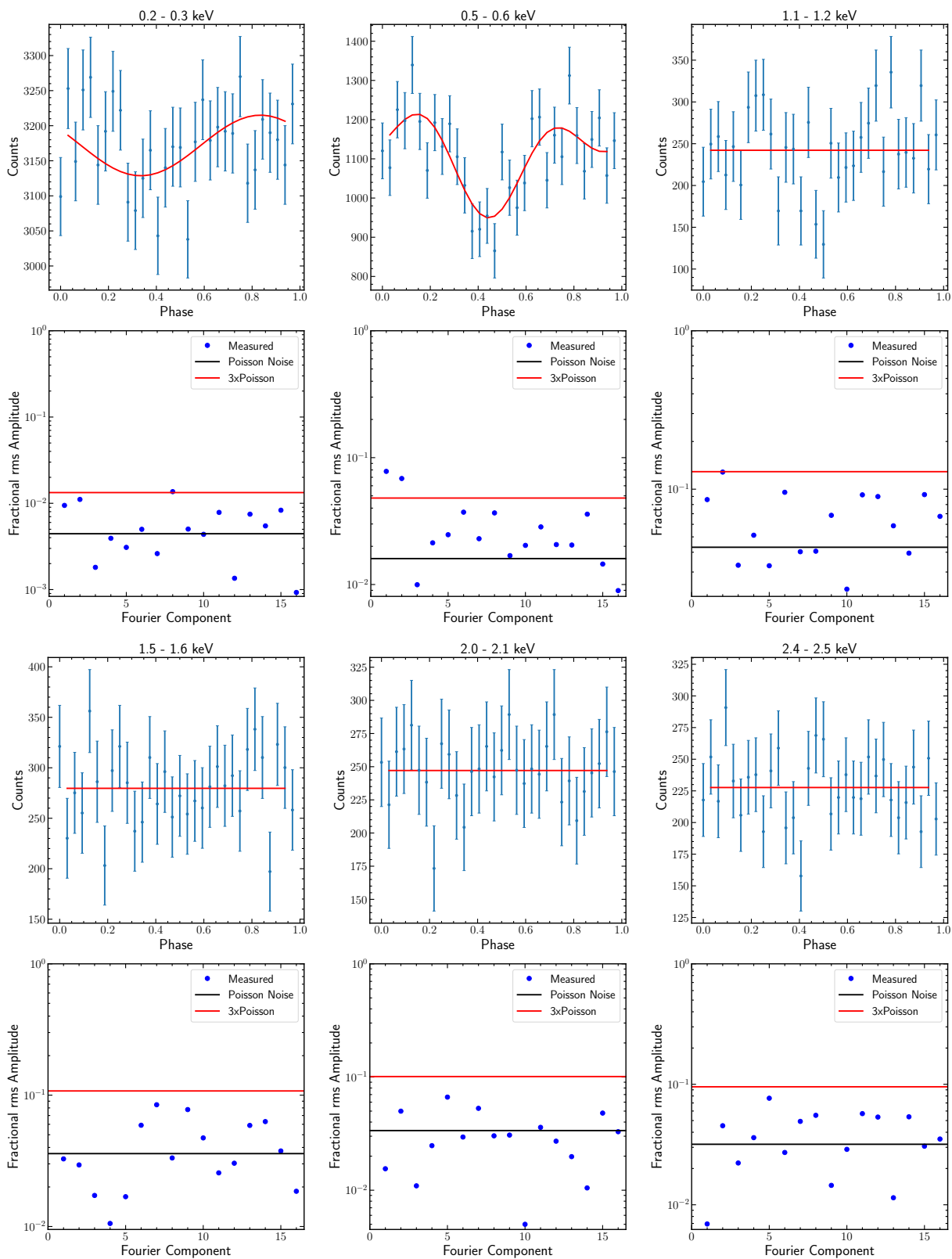


Figure B5. Same as Figure 1 but for PSR J0740+6620. For this pulsar, pulsations are only detected between 0.4-1 keV.

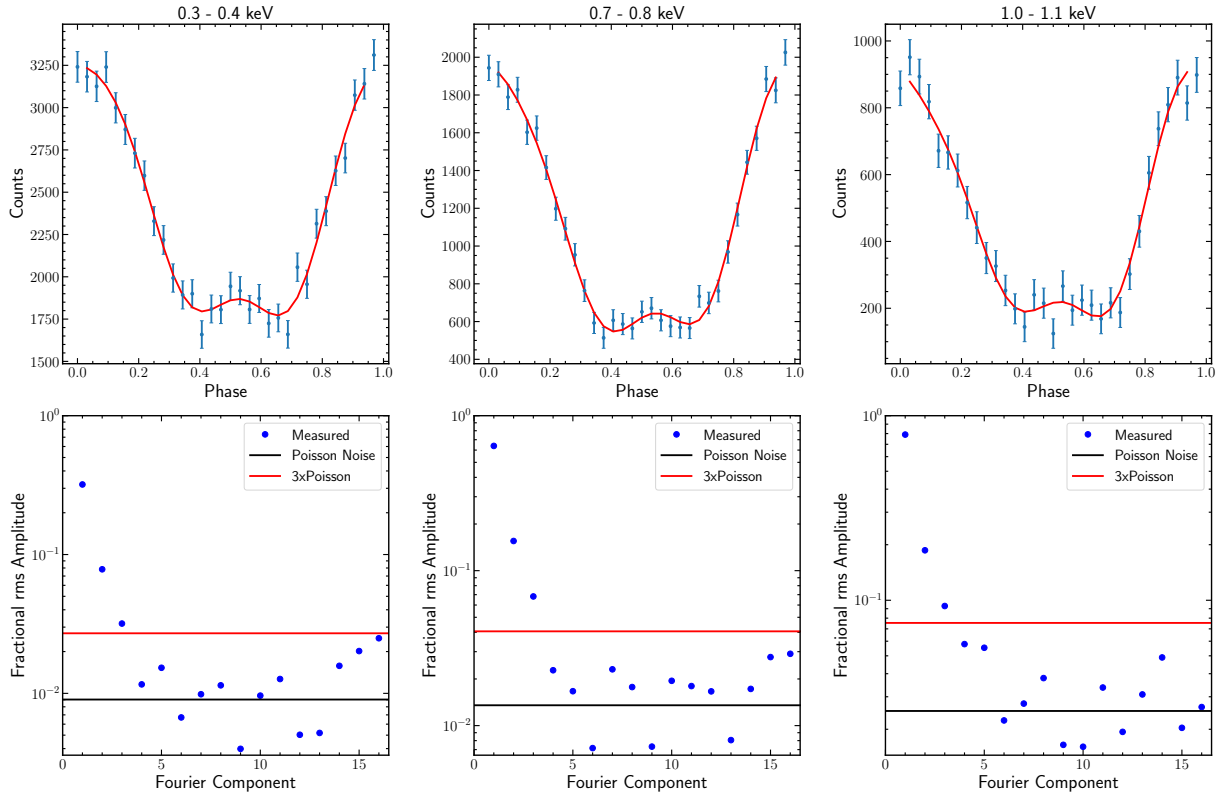


Figure B6. Same as Figure 1 but for PSR J1231–1411. Beyond 1.3 keV, the subtraction of the background results in no net source counts.

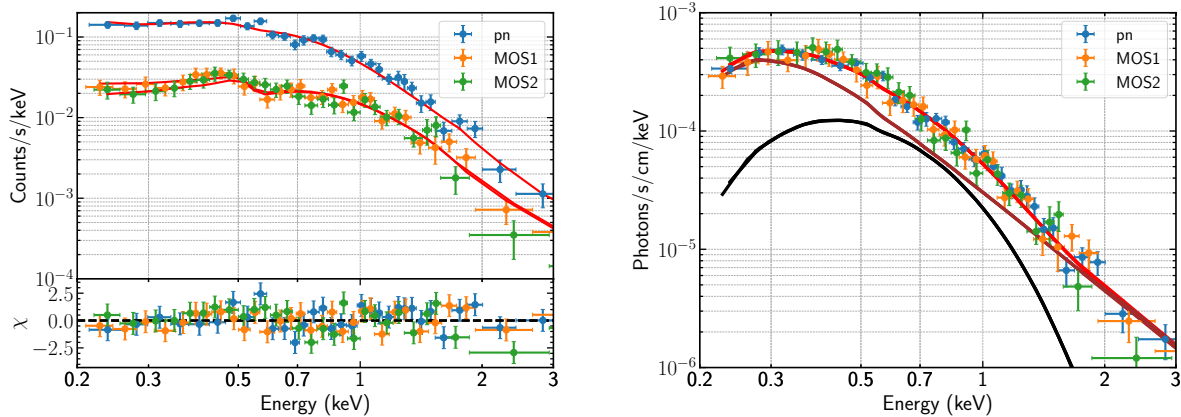


Figure B7. X-ray spectrum of PSR J1231–1411 obtained with *XMM-Newton*. The left panel shows the data and the best fit model (upper panel) together with the residuals (lower panel). The right panel shows the model components, which contain an absorbed blackbody (black) and a power-law component (red).